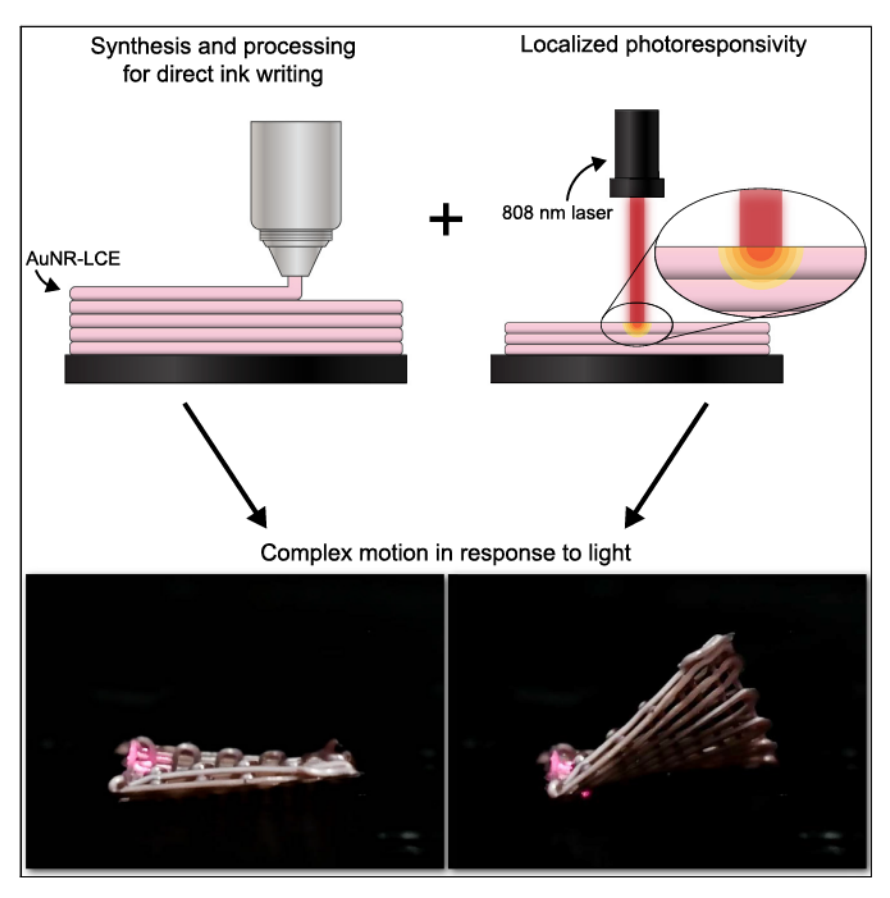
# **Matter**



### **Article**

# Movement with light: Photoresponsive shape morphing of printed liquid crystal elastomers



In this paper, Ford et al. describe multifunctional material development for additive manufacturing. By controlling formulation properties and optimizing inks, they demonstrate precise 3D printing of gold nanorod/liquid crystal elastomer composites with spatiotemporal control. These structures exhibit unique photoresponsive actuation, showcasing novel modes of movement, including oscillation and transportation of mass in response to light. The study marks progress in creating 3D-printed, intelligent materials with applications in soft robotics and biomedical devices.

Michael J. Ford, Dominique H. Porcincula, Rodrigo Telles, ..., Shu Yang, Elaine Lee, Caitlyn C. Cook

krikorian3@llnl.gov (C.C.C.) lee1040@llnl.gov (E.L.)

#### Highlights

Optimized inks for additive manufacturing of a liquid crystal elastomer composite

Developed spatiotemporal control during printing for complex three-dimensional structures

Demonstrated unique combinations of complex threedimensional photoresponsive actuation

Controlled novel modes of actuation with computer vision techniques



## **Matter**



#### **Article**

# Movement with light: Photoresponsive shape morphing of printed liquid crystal elastomers

Michael J. Ford,<sup>1</sup> Dominique H. Porcincula,<sup>1</sup> Rodrigo Telles,<sup>3</sup> Julie A. Mancini,<sup>1</sup> Yuchen Wang,<sup>2</sup> Mehedi H. Rizvi,<sup>4</sup> Colin K. Loeb,<sup>1</sup> Bryan D. Moran,<sup>1</sup> Joseph B. Tracy,<sup>4</sup> Jennifer A. Lewis,<sup>3</sup> Shu Yang,<sup>2</sup> Elaine Lee,<sup>1,\*</sup> and Caitlyn C. Cook<sup>1,5,\*</sup>

#### **SUMMARY**

Soft machines will require soft materials that exhibit a rich diversity of functionality, including shape morphing and photoresponsivity. The combination of these functionalities enables useful behaviors in soft machines that can be further developed by synthesizing materials that exhibit localized responsivity. Localized responsivity of liquid crystal elastomers (LCEs), which are soft materials that exhibit shape morphing, can be enabled by formulating composite inks for direct ink writing (DIW). Gold nanorods (AuNRs) can be added to LCEs to enable photothermal shape change upon absorption of light through a localized surface plasmon resonance. We compared LCE formulations, focusing on their amenability for printing by DIW and the photoresponsivity of AuNRs. The local responsivity of different three-dimensional architectures enabled soft machines that could oscillate, crawl, roll, transport mass, and display other unique modes of actuation and motion in response to light, making these promising functional materials for advanced applications.

#### INTRODUCTION

Soft machines could enable new breakthroughs in technologies related to human-machine interactions, remote exploration in difficult-to-reach spaces, and individually tailored health care. These machines will require soft materials that exhibit a diverse range of functionalities, including actuation for movement, conductivity for sensing and signal processing, stimuli-responsivity, self-healing, and reprocessability. <sup>1–3</sup> The demonstration of such a diverse range of functionalities results in a profound outcome where "the material is the machine." <sup>4,5</sup> That is, by taking advantage of behaviors like self-assembly and phase transitions, these materials as machines can replace traditional sensors, transducers, gears, levers, and electromagnetic motors to enable perception, responsivity, and motion without engineered complexity.<sup>2,4</sup>

Liquid crystal elastomers (LCEs) that are pre-programmed to change shape in response to external stimuli are considered useful for soft machines. <sup>6,7</sup> The shape morphing is induced by heat, electricity, and light. <sup>8,9</sup> Light may be useful to stimulate localized actuation and does not require physical contact with the shape-changing material, as wires that transmit electrical power might require. <sup>10,11</sup> Localized actuation using light could also allow for unique modes of actuation. <sup>12</sup> For example, asymmetric illumination of photoresponsive LCEs led to twisting and rolling motions. <sup>13</sup> Peristaltic motion that resembles the movement of biological organisms has been demonstrated by using localized impingement of different patterns of light

#### **PROGRESS AND POTENTIAL**

Soft matter that can adapt in response to a stimulus like light holds immense promise for various applications, such as biomedical devices and soft robotics. One example of adaptive soft matter is liquid crystal elastomer composites, which incorporate a functional additive and change shape through a phase transition. The combination of the material composition, the printed geometry of the material, and the localization of the stimulus can enable novel movement and reaction to light, as we demonstrate in this paper. Our results mark a significant advancement toward creating complex, 3D-printed, intelligent materials that pave the way for developing next-generation adaptive machines and devices that can transform in response to specific stimuli.





upon an LCE. <sup>14</sup> To extend this work, the programmed order of the liquid crystal (LC) domains could be controlled and modified. The combination of continued development of LCEs with light responsivity and localized actuation of these materials may be important for actuation that is activated at a distance, such as for search and rescue or medical robots or devices, which will require movements that enable locomotion to perform useful work.

Photothermal actuation is a common route to achieve movement with light. Compared with photoswitchable actuation, which relies on chromophores like azobenzene derivatives that change molecular conformation upon absorption of light, 15-17 photothermal actuation relies on the conversion of light to thermal energy. 18,19 When the temperature increases above the nematic-to-isotropic transition temperature (T<sub>NI</sub>), the LCE shrinks in the aligned direction and expands in the direction perpendicular to the alignment. Early reports on LCEs capable of photothermal actuation used composites of carbon nanotubes (CNTs) and LCEs to induce bending or linear actuation with infrared (IR) light.<sup>20–22</sup> LCE-CNT composites can actuate using light sources that have low surface power density (<0.280 W cm<sup>-2</sup>).<sup>23</sup> Other functional fillers like MXenes have also been explored to introduce photoresponsivity into LCEs.<sup>24</sup> However, one challenge with the inclusion of rigid fillers like CNTs in the soft LCE matrix is that the actuation strain of the LCE can be hindered. 25,26 Thus, there is a trade-off between responsivity, which may increase when loading a high-volume content of rigid fillers, and LCE actuation strain, which may decrease at high-volume content of rigid fillers. In addition, CNTs may be useful when broadband absorption is suitable, but CNTs lack selectivity of the wavelength that stimulates the photothermal effect. Functional fillers like gold nanorods (AuNRs) that can absorb strongly at specific wavelengths and allow for photoresponsivity at low-volume loadings are attractive alternatives.<sup>27</sup> The ability to absorb at specific wavelengths can also be advantageous compared with photoresponsivity with chromophores that allow for photoswitchable actuation.

The absorption range of AuNRs can be tuned by tuning their dimensions and aspect ratios. <sup>27</sup> In LCEs, AuNRs have been incorporated to enable photothermal responsivity. An early report described stabilizing AuNRs using thiol-based polymers that could also be coupled with LC moieties to form LCEs, which allowed for the production of fiber actuators that could reversibly actuate, lifting and lowering an object. <sup>28</sup> More recent reports expanded functionality and explored the material properties of AuNR-LC composites. <sup>29,30</sup> For example, AuNRs can also be used with photoswitchable chromophores to enable multiresponsivity. <sup>31</sup>

Additive manufacturing of LCEs has become an important technique for LCE processing, and the advantages of additive manufacturing should be considered to maximize functionality.<sup>32</sup> Specifically, direct ink writing (DIW) of LCEs can align mesogens via shear forces, permitting reversible shape change.<sup>33</sup> Since the initial demonstrations of shear-aligned LCEs by DIW,<sup>34–36</sup> exploration of LCE printing has proliferated.<sup>37</sup> LCE architectures that have been printed include lattice structures, structures with Gaussian curvature, robotic materials with hinges, and more.<sup>34,38,39</sup> Investigations of printable LCE formulations that incorporate stimulus-responsive additives are less common but still important, especially to enable new functionalities that could expand utility. Some examples of investigations include the incorporation of magnetic particles<sup>40</sup> and metals that are liquid at room temperature.<sup>41,42</sup> Notably, the synthesis and curing of the LC ink, the actuation properties of the LCE composite, and the responsivity in the presence of the stimulus-responsive filler must all be considered when optimizing inks for a specific

<sup>&</sup>lt;sup>1</sup>Lawrence Livermore National Laboratory, Livermore, CA 94550, USA

<sup>&</sup>lt;sup>2</sup>Department of Materials Science and Engineering, University of Pennsylvania, 3231 Walnut Street, Philadelphia, PA 19104, USA

<sup>&</sup>lt;sup>3</sup>John A. Paulson School of Engineering and Applied Sciences and Wyss Institute for Biologically Inspired Engineering, Harvard University, Cambridge, MA 02138, USA

<sup>&</sup>lt;sup>4</sup>Department of Materials Science and Engineering, North Carolina State University, Raleigh, NC 27695, USA

<sup>&</sup>lt;sup>5</sup>Lead contact

<sup>\*</sup>Correspondence: krikorian3@llnl.gov (C.C.C.), lee1040@llnl.gov (E.L.)

https://doi.org/10.1016/j.matt.2024.01.006





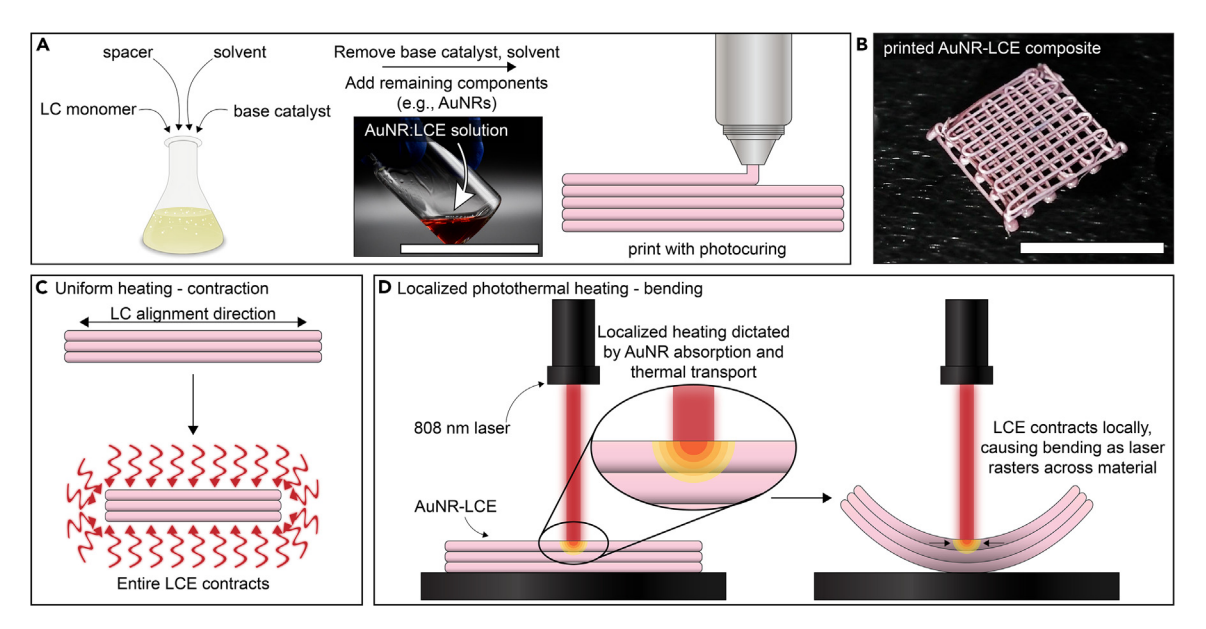


Figure 1. Tailoring LCE photoresponsivity

- (A) Illustration of formulation scheme, following the synthesis of the oligomer precursors, the addition of AuNRs, and the printing of the formulation.
- (B) Photograph of printed lattice structure of a LCE formulation that contains AuNRs.
- (C) Illustration of how uniform heating results in contraction.
- (D) Illustration of how localized heating could result in modes of actuation that are different from uniform heating for a given printed structure.

printing method. Furthermore, the print architecture in combination with the filler responsivity will dictate material functionality and, ultimately, utility.

We posit that the controlled dispersion of AuNRs in LCE matrices should enable reliable photothermal shape morphing of 3D-printed architectures. By introducing a thiol-terminated poly(ethylene glycol) (PEG) polymer to functionalize AuNRs, researchers recently demonstrated the uniform dispersion of these AuNRs.  $^{43,44}$  AuNRs have also been incorporated into resins tailored for light-based 3D printing, leading to new geometries and modes of reversible actuation.  $^{45,46}$  Each resin (or ink) must be carefully optimized for the specific additive manufacturing technique used. For example, while LCEs were printed via two-photon polymerization with feature sizes less than 50  $\mu m$ , no actuation was demonstrated.  $^{45}$  By contrast, direct laser writing coupled with the use of an alignment layer leads to patterned LCEs that exhibit shape morphing.  $^{47}$ 

In this paper, we report the creation of AuNR-filled LCE inks for DIW and demonstrate the fabrication of photoresponsive materials that exhibit the requisite actuation response needed for locomoting soft machines controlled via computer vision techniques. We determined the advantages and disadvantages of different ink formulations by characterizing their curing kinetics, molecular weight, and rheological and thermal properties (Figures 1A and S1). We considered two possible routes for formulating inks and identified thiol-based oligomers that possessed fast curing kinetics at room temperature, allowing for on-demand rheological control with ultraviolet (UV) light during DIW. Next, we selected inks that appeared promising for DIW and evaluated their amenability to printing and the actuation characteristics of the printed materials. Finally, we added AuNRs to an acrylate-terminated oligomer matrix (Figure 1B) and characterized their photothermal responsivity. These printed structures exhibited the desired shape-morphing behavior in response to incident heat or light. When heated uniformly, their actuation was determined by the





programmed shear-induced LC alignment during printing. For example, a printed rectangular bar that is uniaxially aligned along a single printing direction will contract in that direction (Figure 1C). By contrast, their photoresponsivity enables localized heating dictated by AuNR absorption and thermal transport. Depending on the incident dosage of light, the LCE can contract locally and actuate like a bilayer actuator, resulting in bending that enables diverse actuation (Figure 1D). Importantly, the localized heating in combination with 3D architectures in complex geometries, such as lattices, enables unique modes of actuation and multiresponsivity for a single material and architecture. Demonstrated modes of actuation include their ability to repeatably oscillate, crawl, roll, and transport mass. Continuous rolling was demonstrated using computer vision techniques that tracked the position of the composite and continuously applied the light stimulus to the sample. Such varied functionality for a single composite was enabled by the composition of the composite, the architecture of the print, and the localization of the stimulus. Altogether, the properties that manifested for these composites are promising for soft machines.

#### **RESULTS AND DISCUSSION**

#### Ink synthesis

We first evaluated differences in synthesis and processing to formulate printable inks that were compatible with AuNRs. For DIW at room temperature, inks should be composed of oligomers that can be reproducibly synthesized, that can flow at room temperature, and that can cure quickly in response to UV light. We considered control of monomer addition, monomer stoichiometry, LC monomer composition, addition of inhibitor, and the effect of solvent drying as factors that could affect reproducibility in the synthesis and rheological properties of the inks. The effects of all factors considered on molecular weight are summarized in Table S1. A previous report that characterized thin films of an LCE/AuNR composite used a mixture of LC monomers and thiol-terminated oligomers to synthesize the films. 44 Then, a followup publication described printing of bilayers of LCE/AuNR composites; in this case, an acrylate-terminated oligomer was used (Figure S1). 46 Thus, comparison and optimization of the printability and material properties of these different formulations may be useful to produce responsive materials for complex printing via DIW. Furthermore, a direct comparison of the compatibility of AuNRs with amine-based LC oligomers is relevant to compare with many prior publications demonstrating DIW using these amine-based oligomers.<sup>33</sup> The trade-offs related to printing and photoresponsivity between these three formulations will be discussed.

LC oligomers that contain the thiol-based monomer ethylene glycol bis(3-mercapto-propionate) (GDMP) were synthesized by reacting the monomers in the presence of a base catalyst, 1,8-diazabicyclo[5.4.0]undec-7-ene (DBU), in solvent (dichloromethane, DCM). A solution that contained the acrylate-terminated monomer (RM82) was added to the solution that contained GDMP and DBU. We varied the rate of monomer addition, which affected molecular weight and viscosity. The addition proceeded either quickly, at a rate of >3.3 mol % s<sup>-1</sup>, or slowly, at a rate that was between 0.06 and 0.15 mol % s<sup>-1</sup>. In this case, acrylate-terminated oligomers were synthesized, targeting an approximate molar ratio of 1.2:1 acrylate:thiol. After removing the base catalyst and drying the solvent, the molecular-weight distributions were characterized using a size-exclusion chromatography (SEC) system that included a multiangle light-scattering (MALS) detector and refractive index detector. The number-average molecular weights (M<sub>n</sub>) were on the order of 10<sup>3</sup> for all oligomers (Table S1). These values of molecular weight are near the limit of detection for this instrument; however, the detection of eluted species based on the change in



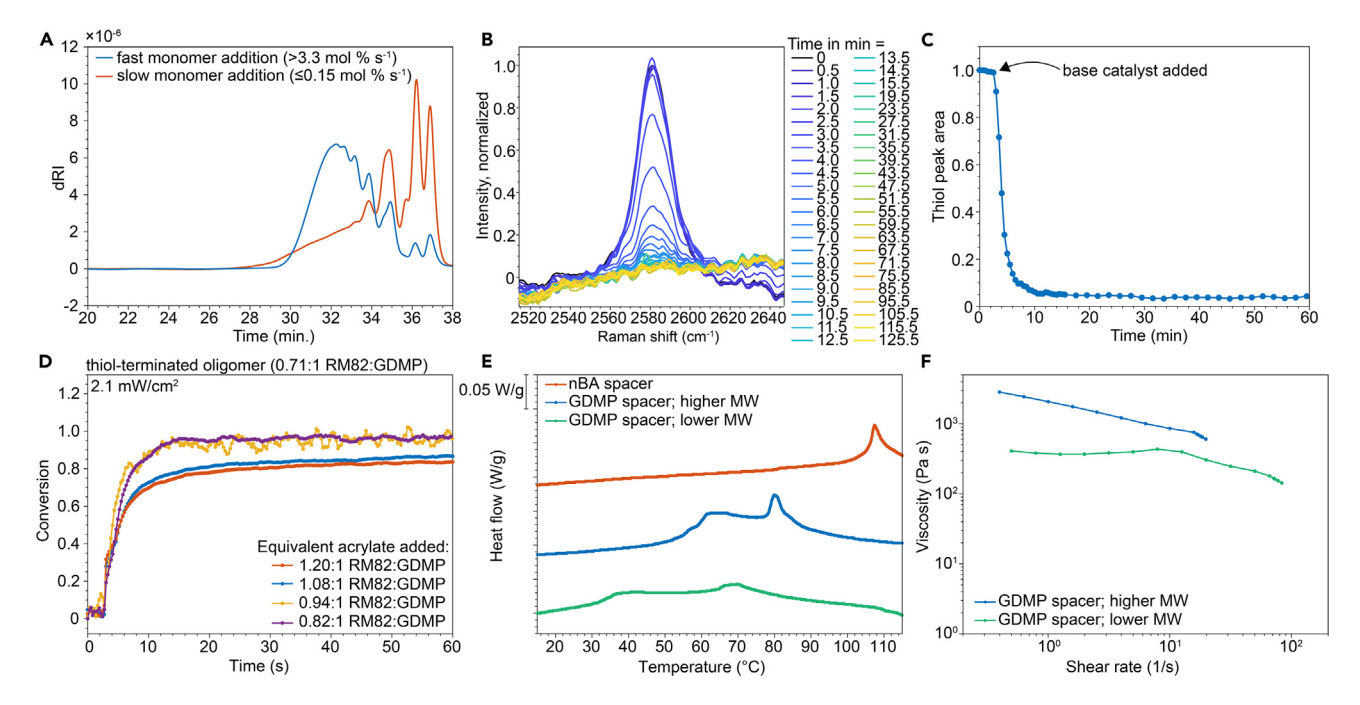


Figure 2. Ink synthesis optimization and characterization

- (A) Elution chromatograms using the differential refractive index (dRI) of two formulations. Both formulations contained 1.2:1 RM82:GDMP but had different processing conditions.
- (B) Raman spectra measured in situ for a 1.2:1 RM82:GDMP formulation where the catalyst was added after mixing monomers.
- (C) Integrated thiol peak area over time for the corresponding in situ Raman monitoring displayed in (B).
- (D) Acrylate conversion as measured by FTIR for acrylate-terminated oligomers that were loaded with different amounts of photoinitiator (PI).
- (E) Thermal transitions upon melting for different LC formulations. Endothermic heat flow is directed upward.
- (F) Shear-dependent viscosity of different LC formulations at room temperature.

refractive index (differential refractive index; dRI) can provide qualitative insight. The faster rate of addition (>3.3 mol % s $^{-1}$ ) resulted in a formulation that contained a higher concentration of oligomers that had larger molecular weights compared with the slower rate of addition (Figure 2A). When characterized by SEC, the largest peak in the dRI occurred at 32.2 min for the formulation synthesized at a faster rate of addition. For this batch,  $M_n$  was 5,363 g/mol. The largest peak occurred at 36.2 min for the formulation synthesized at a slower rate of addition, and the  $M_n$  was 2,342 g/mol.

We observed that the slower rate of addition (0.06–0.15 mol % s $^{-1}$ ) resulted in larger concentrations of lower molecular weight species, since the dRI can be associated with concentration. These lower molecular weight species can be distinguished as sharp peaks, as they are separated by discrete molecular weight values. This observation was repeatable for multiple batches (Figure S2; Table S1). For seven batches where LC monomer was added slowly, the average  $M_n$  was 2,386  $\pm$  603 g/mol. For six batches where LC monomer was added quickly, the average  $M_n$  was 4,157  $\pm$  1,012 g/mol. Other processing effects also influenced  $M_n$  and the weight-average molecular weight ( $M_w$ ), and  $M_w$  varied more than  $M_n$  between batches, possibly due to homopolymerization of the LC monomer during drying (Table S1). These differences in molecular weight, which would have an impact on viscosity and thus printability, could be explained by the difference in addition rate.

We examined the conversion of the functional groups during the addition of monomer using *in situ* Raman spectroscopy, where a Raman probe could be directly





inserted into our reaction vessel to observe the oligomerization kinetics. The conversion of thiols on GDMP was determined using the Raman signal at  $\approx 2,580$  cm<sup>-1</sup>. The sensitivity of our in situ characterization was deemed suitable to track the conversion of thiols (Figure S3). First, thiol- and acrylate-based monomers were added to DCM. The Raman signal of the thiol peak was monitored for ≈ 2.5 min to establish a baseline. Then, the base catalyst DBU was added while stirring. The area of the thiol peak decreased quickly, reaching <10% of its original peak area within 4 min (Figures 2B and 2C). The area of the peak that corresponds to the acrylate group at  $\approx 1,635$  cm<sup>-1</sup> decreased concomitantly. The precipitous decrease in peak area indicates that the thiol and acrylate coupling occurs quickly after adding catalyst. The  $M_n$  for this polymerization was 7,818 g/mol, and the distribution was similar to the distribution for the fast monomer addition (Figure S2). Similarly, the thiol conversion occurred quickly when RM82 was added at different rates to a solution that contained GDMP and DBU (Figure S3). While initial thiol conversion occurred quickly in all cases, the molecular weight distribution was distinctly different, resulting in a difference in the viscosity between materials made with different monomer addition rates. One possible cause for this difference relates to the inability to form long chains when high concentrations of thiols are present with low concentrations of acrylates as in the case for the slower addition of monomers. The thiols react quickly with the acrylates, forming a low concentration of trimers (i.e., thiol-acrylate-thiol). Since these trimers exist in low concentrations, they are less likely react to form longer oligomers when more acrylate is added. As additional acrylate is added, the thiol monomers will continue to react rather than the trimers until the concentration of trimers is higher than the concentration of thiol monomers. At this stage, pentamers may start to form, but these larger molecules will also be in low concentration relative to the remaining monomers and trimers. After reaching a stoichiometric balance of 1:1 thiol:acrylate, there would be a high concentration of short oligomers due to the slower addition of monomer. Further addition of monomer would be less likely to react with unreacted thiol, as the concentration of unreacted thiol would be low. Indeed, by comparing the elution of RM82 by itself, we observed that the eluted peak overlaps with a peak that is observed in the ink formulations (Figure S2D). This peak is much larger for synthesis with a slow addition of monomer, indicating a higher concentration of low molecular weight acrylates in these formulations compared with formulations with a faster addition. Examination of the  $M_n$  and the molecular mass of the monomers showed that pentamers that are acrylate terminated would have a molecular mass of around 2,500 g/mol. With slower addition of monomer,  $M_n$  is 2,386  $\pm$ 603 g/mol, and the chromatogram shows peaks for distinct functional units (e.g., monomers, trimers).

For comparison, the synthesis of LC oligomers that contain amine-based monomers may be viewed as simpler than the synthesis of those that contain thiol-based monomers. Often, these amine-containing oligomers are made in a single reaction vessel and do not require the removal of catalyst nor solvent, which can complicate processing and/or cause unintended polymerization of functional groups (Figures S4–S6). However, further comparison of curing kinetics of the oligomers for DIW, formulation properties, and AuNR compatibility was considered necessary to evaluate the suitability of these formulations.

#### **Curing kinetics**

The curing kinetics of these formulations were monitored by measuring the near-IR response as the formulations were exposed to UV illumination, which mimicked curing during DIW. The conversion of acrylate functional units was compared for all formulation types considered here: (1) thiol-terminated oligomers with the



remainder stoichiometric balance of LC monomer added; (2) acrylate-terminated oligomers that use GDMP as a spacer; and (3) acrylate-terminated oligomers that use n-butylamine (nBA) as a spacer (Figure S1). These formulations will be designated as Th-LCE, A-LCE-Th, and A-LCE-Am, respectively. First, LC monomer was dissolved in Th-LCE and conversion was monitored. Here, the conversion occurred quickly, reaching 96% conversion after 30 s, depending on the amount of LC monomer dissolved in Th-LCE (Figure S7). Like Th-LCE with excess acrylate, the A-LCE-Th with stoichiometry of 1.2:1 RM82:GDMP cured quickly, reaching >90% conversion within 30 s when the photoinitiator (PI) content was >1 wt %. (Figure 2D). In comparison to the A-LCE-Th and Th-LCE, the A-LCE-Am cured much more slowly at room temperature. This formulation did not reach 50% curing until after about 60 s. Further discussion of these curing kinetics is provided in Figures S7 and S8. Following these studies of curing kinetics, the remaining formulations studied were those that contained the acrylate-terminated oligomers (A-LCE-Th and A-LCE-Am), primarily due to considerations related to solubility as discussed in the supplemental information.

Formulations that cure more quickly may be useful for printing complex 3D structures that bridge gaps. Conversely, curing that is too quick may clog the printing nozzle or result in poor adhesion between layers. These trade-offs can be partially controlled by controlling the surface power density of the UV exposure during curing, but the curing kinetics also play a meaningful role. Overall, any difference in curing may also be related to oligomer mobility, which may be affected by molecular weight and thermal properties. Thus, the next consideration for these formulations was their thermal and rheological properties.

#### Thermal and rheological properties

The thermal transitions of the different formulations were tracked using differential scanning calorimetry (DSC). A-LCE-Am had a single transition, the  $T_{\rm NI}$ , at  $105^{\circ}$ C (Figure 2E). Conversely, the A-LCE-Th formulations had multiple thermal transitions, and the onset of these transitions depended on the molecular weight distribution of the formulation. For a formulation that had a higher molecular weight, the  $T_{\rm NI}$  appeared as a sharp transition at  $79^{\circ}$ C. This transition followed a broad transition that began at about  $58^{\circ}$ C. For a formulation that had a lower molecular weight, the  $T_{\rm NI}$  onset was  $62^{\circ}$ C, and this formulation had an initial transition that began at a lower temperature of  $32^{\circ}$ C. The transition that occurred at lower temperatures was not a glass transition temperature, as confirmed by using modulated DSC, which can distinguish between reversing and non-reversing heat flows (Figure S9). The depression of the thermal transitions of LC oligomers relative to their corresponding LC monomer has been attributed to the flexibility of the spacer for a given LC oligomer. These results also suggest that oligomer packing may be affected by molecular weight, where spacers in shorter oligomers could more easily disrupt LC ordering.

Another aspect that is affected by the molecular weight is the rheological properties of these formulations. Oscillatory and constant shear measurements were performed. A-LCE-Th formulations were subjected to oscillatory shear at different temperatures. The onset of a sudden change in storage modulus occurred at temperatures that were associated with the transitions that were observed by DSC (Figure S9). The viscosity was measured at various shear rates, and the thiol-based formulations exhibited shear thinning behavior. The viscosity of the formulation that was higher molecular weight was higher than the viscosity of the formulation that was lower molecular weight (Figure 2F). At a shear rate of 1 s<sup>-1</sup>, the viscosity decreased from 2,080 Pa s at higher molecular weight to about 370 Pa s at lower



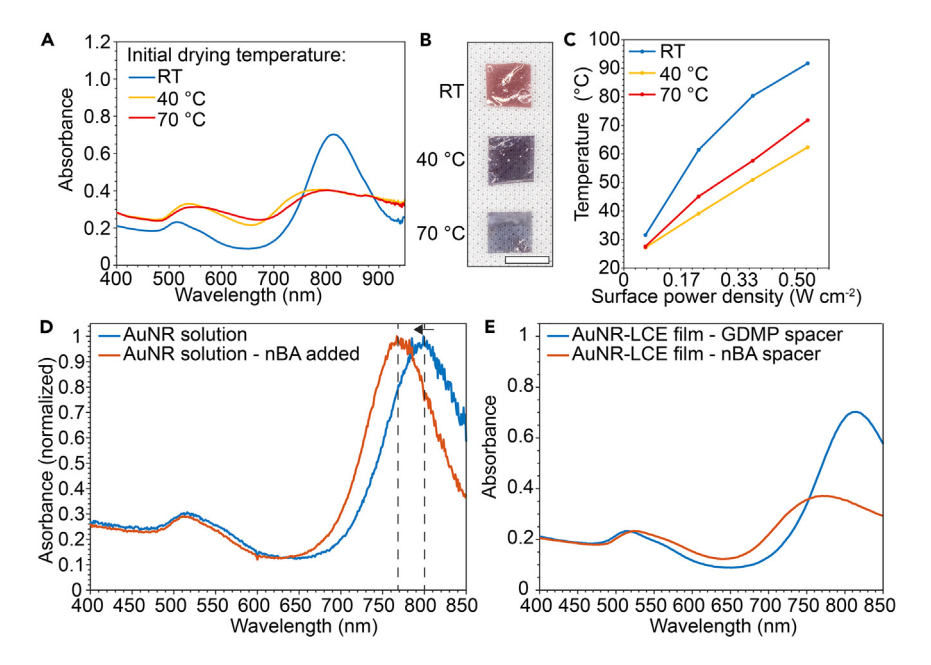


Figure 3. AuNR formulation compatibility and absorbance characteristics

- (A) Absorbance of films that contain AuNRs in LCEs cured from acrylate-terminated oligomers.
- (B) Drying at different temperatures resulted in films with different absorbance and appearance as evidenced in the photograph. Scale bar, 5 mm.
- (C) The differences in absorbance resulted in differences in photothermal responsivity when the steady-state temperature was measured using a thermal camera while LCE films were irradiated with an 808 nm laser.
- (D) Absorption of solutions of AuNR in DCM with and without nBA added. The dashed lines are guides to highlight the shift in maximum absorbance, which is influenced by the aggregation of AuNRs.
- (E) Absorption of thin films of AuNRs in LCE with different spacer units, which shows a shift in maximum absorbance for nBA.

molecular weight. This lower viscosity was deemed suitable for printing at room temperature, so lower molecular weight formulations that were formed by slow addition of acrylate-functional monomer were synthesized for printing. In addition, the differences in viscosity may be one factor that explains the differences in curing kinetics that we observed between formulations that had different molecular weights. Overall, the ability to control viscosity is important for DIW; the viscosity will dictate the pressure required to achieve a given flow rate and will also have an impact on the level of printing complexity that can be achieved.

#### Gold nanorod compatibility

The last property to consider before selecting a formulation for DIW is the photoresponsivity when AuNRs are added. LC oligomers were mixed with AuNRs that were modified with monothiol-terminated PEG (PEG-thiol) and concentrated in DCM. For a formulation that contained GDMP, we observed that the initial processing temperature affected the dispersion of AuNRs. When drying at room temperature, thin films exhibited a strong absorbance at around 815 nm and appeared red (Figures 3A and 3B). When the initial drying was at elevated temperatures (40°C and 70°C), the absorbance at 815 nm decreased to about 60% of the value of the film dried at room temperature. Importantly, the peak wavelength for the films processed at elevated temperatures shifted, which is an indication of aggregation of the AuNRs. These films appeared purple or gray. These films were exposed to an 808 nm laser at varying power for 60 s, and the maximum temperature of the films was measured to



determine the effect of this change of absorption on the photothermal properties (Figure 3C). As the laser power increased, the maximum temperature of the film that was dried at room temperature increased from 32°C at 0.07 W cm $^{-2}$  to 92°C at 0.53 W cm $^{-2}$ . For comparison, the films processed at 40°C and 70°C reached temperatures of 62°C and 72°C at 0.53 W cm $^{-2}$ . These differences in photothermal responsivity highlight the need to control processing parameters (i.e., drying temperature). However, we noted that the viscosity is also affected by drying conditions. These effects appear to be in opposition; however, the discoloration and reduction of optical density for films that are dried at elevated temperatures can be avoided by first drying at room temperature until the composite ink is viscous (e.g., >12 h). Then, elevated temperatures do not affect the dispersion of AuNRs, presumably due to limited mobility in the viscous medium.

The photothermal responsivity was also measured for LC films under conditions that would be mimicked in printing (i.e., at 0.1 wt % AuNRs, which was previously found to be suitable for photothermal actuation of LCEs<sup>44</sup>). A comparison was made between amine-based and thiol-based spacers (A-LCE-Am vs. A-LCE-Th). In addition, an unfilled LCE was measured as a control. For these films, the formulation with the thiol-based spacer had the best photothermal response, reaching temperatures  $>100^{\circ}$ C at a laser surface power density of 0.68 W cm<sup>-2</sup>. For comparison, the formulation with the amine-based spacer reached 64°C at a power of 0.68 W cm<sup>-2</sup> (Figure \$10). This film did not show the same degree of discoloration observed for LCE composites that were dried at elevated temperatures. The LCE film without AuNRs did not exhibit any change in temperature at this same power and increased to 6°C above room temperature (28°C) after being subjected to a laser surface power density of  $3.54 \,\mathrm{W}\,\mathrm{cm}^{-2}$  (Figure S10A). The photothermal response of the AuNRfilled inks demonstrates compatibility of the AuNRs with the different oligomers. In addition to optical properties, we also examined the effect of AuNRs on curing, viscosity, and mechanical properties to confirm that the AuNRs at 0.1 wt % had properties similar to those of the unfilled LCEs (Figure \$10).

Composites that used the A-LCE-Th formulation demonstrated better photoresponsivity than the composites that used the A-LCE-Am formulation. However, compatibility with A-LCE-Am could be improved, as it is clear from these investigations that processing parameters also play a meaningful role in photoresponsivity. To further test this incompatibility, we measured the absorbance of a solution of AuNRs in methyl ethyl ketone (MEK) and then measured the absorbance again after adding about 5 wt % of nBA. The peak wavelength shifted after the addition of nBA, and this shift was similar to shifts observed when comparing thin films of LCEs that used nBA as a spacer vs. those that used GDMP as a spacer (Figures 3D and 3E). Note that this shift is indicative of aggregation of the AuNRs and affects photothermal responsivity. Formulations that used nBA as a spacer may be advantageous for some aspects (e.g., for simple processing that does not require solvent removal). However, based on the photothermal response and fast curing kinetics at room temperature (Table S2), the A-LCE-Th formulation was selected for DIW. Overall, these inks seemed promising to produce complex structures that could be photothermally actuated.

#### Direct ink writing and photothermal actuation

Samples were printed by extruding the viscous inks through a nozzle and curing using a UV source incident upon the ink (Figure S11A). The fast curing allowed for high fidelity in printed structures. The ink could span wide gaps and cure in place with minimal sagging when curing conditions were optimized (Figure 4A).



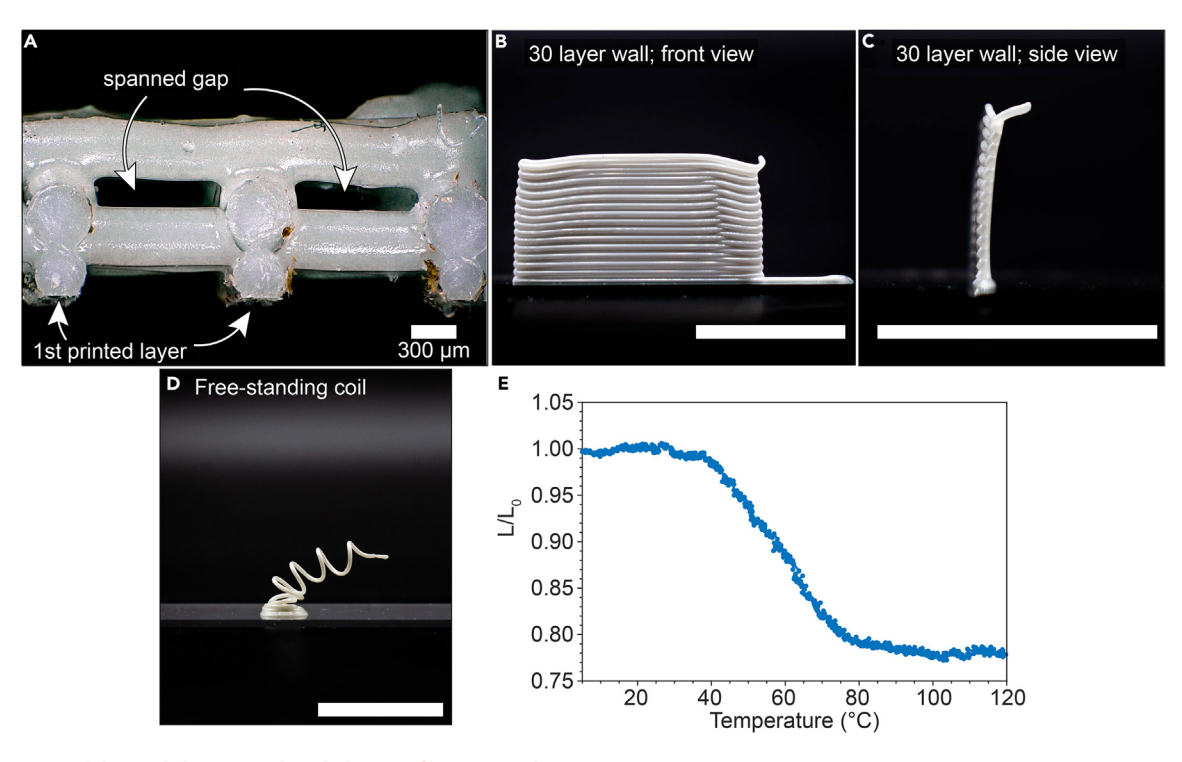


Figure 4. Printability and shape-morphing behavior of pure LCE inks

(A) Micrograph of a side view of a printed structure, demonstrating the ability of the inks to span a wide gap.
(B and C) Front view (B) and side view (C) of a printed structure that is 30 layers tall and 1 layer wide.
(D) A printed coil that was formed by curing an unsupported ink strand. A base cylinder was deposited first.
(E) Example of normalized actuation strain measured at 0 N tension through the nematic-to-isotropic transition temperature. Dashed lines are for reference. The scale bars in (B)–(D) represent 15 mm.

In addition, we printed a tall structure (30 layers) that was a single filament wide. This structure showed noticeable sagging on the edges after multiple layers were printed, but the structure stayed upright while the ink continued printing (Figures 4B and 4C; Video S1). Fast curing also allowed for printing of coiled structures by curing unsupported strands of ink (Figure 4D; Video S1). Both rectangular bars (Figures S11B and S11C) and lattice structures (Figures S11D and S11E) were also printed and characterized. Samples that exhibited typical shear alignment after printing contracted upon heating. The rectangular bar contracted to about 74% of its original length (Video S2). The lattice structure contracted to about 76% of its original area (Video S2). As the lattice cools, the pores shrink. The difference in the contraction of the lattice structure compared with the bar may be due to differences in printing parameters, ink formulation, and geometric constraints. Other rectangular bars were also characterized by measuring their length using a dynamic mechanical analyzer. For samples that exhibited linear contraction at a tension of 0 N, the normalized actuation strain (L/L<sub>0</sub>, where L<sub>0</sub> is the length at 20°C) ranged from about 0.91 to 0.77 when considering L at 120°C (Figure 4E). These values of contraction are within the range of previously reported inks of similar composition. The variation may be due to the printing parameters and variations between batches.46

A printed solid bar structure that contained AuNRs exhibited good photoresponsivity and reached higher temperatures at lower laser power than thin films, likely due to poorer heat dissipation of the solid structure compared with the films (Figure 5A). At input surface power density of 0.83 W cm<sup>-2</sup>, the sample reached





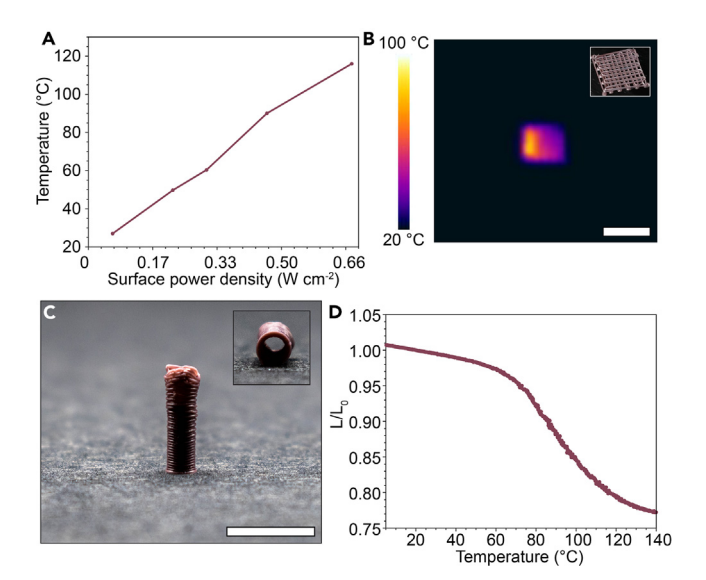


Figure 5. Printability and shape-morphing behavior of AuNR-filled LCE inks

- (A) Thermal responsivity of printed and infilled AuNR-LCE composite.
- (B) Thermal image of a printed lattice structure (inset). The laser had just rastered the leftmost edge of the composite.
- (C) Single filament cylinder that is  $>3 \times$  taller than its diameter. The inset shows the cylinder on its side to show the single-filament walls.
- (D) Normalized actuation strain of a AuNR-LCE composite measured at 0 N tension through the nematic-to-isotropic transition temperature. The scale bars represent 15 mm.

temperatures >150°C, which were above the limit of detection of our thermal camera. When the laser rastered across a printed composite, localized heating was observed, demonstrating the photoresponsivity (Figure 5B). Conversely, when the laser rastered across a printed LCE that did not include AuNRs, no shape change was observed (Video S3). Tall structures, like a single-filament cylinder (Figure 5C), and structures in which strands that span gaps could be printed, highlighting how the use of AuNRs does not disrupt the fast kinetics of curing. Importantly, the inclusion of AuNRs should not disrupt the linear actuation of printed rectangular bars. The normalized actuation strain was measured for bars that contained 0.1 wt % AuNRs, reaching a value of 0.79 considering L at 120°C (Figure 5D). This value was within the range that we measured for unfilled LCEs and is consistent with previous reports that incorporated AuNRs in LCEs. 44,46

Next, we printed structures to explore the combined effect of printed 3D geometry and localized photothermal stimulation on the actuation capabilities. We printed a solid bar and three different lattice structures (90°, 45°, and gyroid), which differed in the localized alignment of LC domains (Figure 6A). The localized photothermal stimulation impinges upon the solid bar, but the light does not transmit through the entire sample, which causes only the top layers to shrink and results in bending (Video S4). This bending can be characterized by the maximum measured curvature, which increases as the surface power density of the laser increases concomitant with an increase in surface temperature (Figure 6B). The resulting curvature appears repeatable; we noticed no meaningful degradation in the curvature after 100 cycles (Figure 6C). Note that for a constant laser stimulus over time, heat can conduct to subsequent layers more quickly than it dissipates to the ambient environment, and the sample will contract as well (Video S4), highlighting an ability to control the actuated shape by controlling the stimulus.



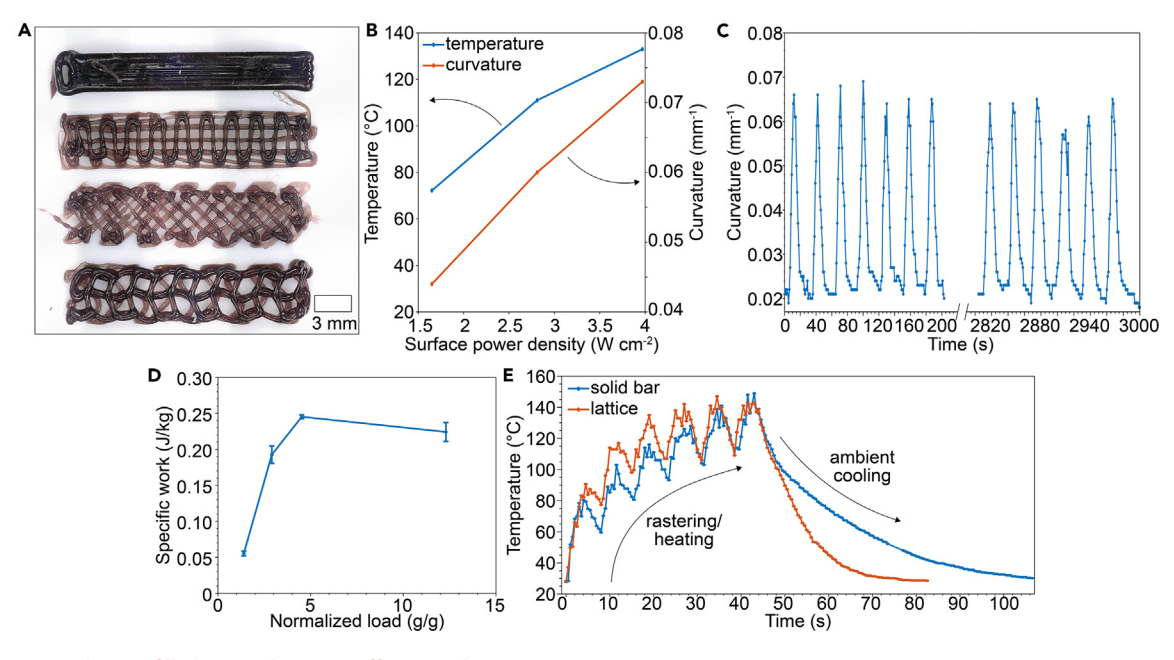


Figure 6. Printed AuNR-filled LCE architecture effects on photoresponsive actuation properties

- (A) Optical images of printed components with similar geometric footprints but different porosity and print patterns that direct liquid crystal alignment. The components from top to bottom are referred to as the solid bar, the 90° lattice, the 45° lattice, and the gyroid lattice.
- (B) Initial curvature and surface temperature of the solid bar as a function of surface power density of the laser.
- (C) Tracking of curvature through 100 cycles for the solid bar, showing the first seven and last six cycles.
- (D) Actuation characteristics of the solid bar, where the bar was anchored on one end and the distance that the mass was lifted was monitored to determine the specific work density. Error bars, SD of at least three measurements.
- (E) Comparison highlighting the faster cooling rate of the 90° lattice in comparison with a solid bar after reaching about 145°C.

We also examined how the composite could do mechanical work by fixing one end and attaching a weight to the other end, allowing the composite to lift the weight when the laser rastered across the sample. The specific work density increased as the load increased (Figure 6D); for a mass that was 4.5 x the mass of the composite, the composite had a specific work density of 0.25 J/kg. For a larger mass that was 12x the mass of the sample, the composite could not lift the mass as high, and the specific work density decreased to 0.22 J/kg. These composites lifting masses that were much larger than the sample mass represent useful work that can be performed by the material. The rectangular components that were printed with different lattice geometries offer an additional example of the utility of these materials and highlight the importance of the printed geometry to the actuation capabilities. First, the solid bar and a 90° lattice were both subjected to a photothermal stimulus that allowed the sample to reach about 145°C. Then, the temperature was measured as the components cooled in the ambient environment (Figure 6E). Due to a greater surface area with the surrounding environment, the 90° lattice reached <32°C after 26 s following laser rastering, whereas the rectangular bar required 59 s to reach <32°C, which would permit quicker responsivity of the composite.

In addition to differences in cooling rates, the modes of actuation that are observed differ as well, and rastering introduces asymmetry into the actuation that results in novel motion. While the solid bar bends away from the surface and then shrinks after continued stimulus (Figure 7A), the lattice structures have more flexibility and can bend in the plane of the surface as well as away from the surface (Video S4). The solid bar exhibits greater maximum curvature during rastering, due to the relative flexibility of the lattice structure. The most interesting observation was the actuation



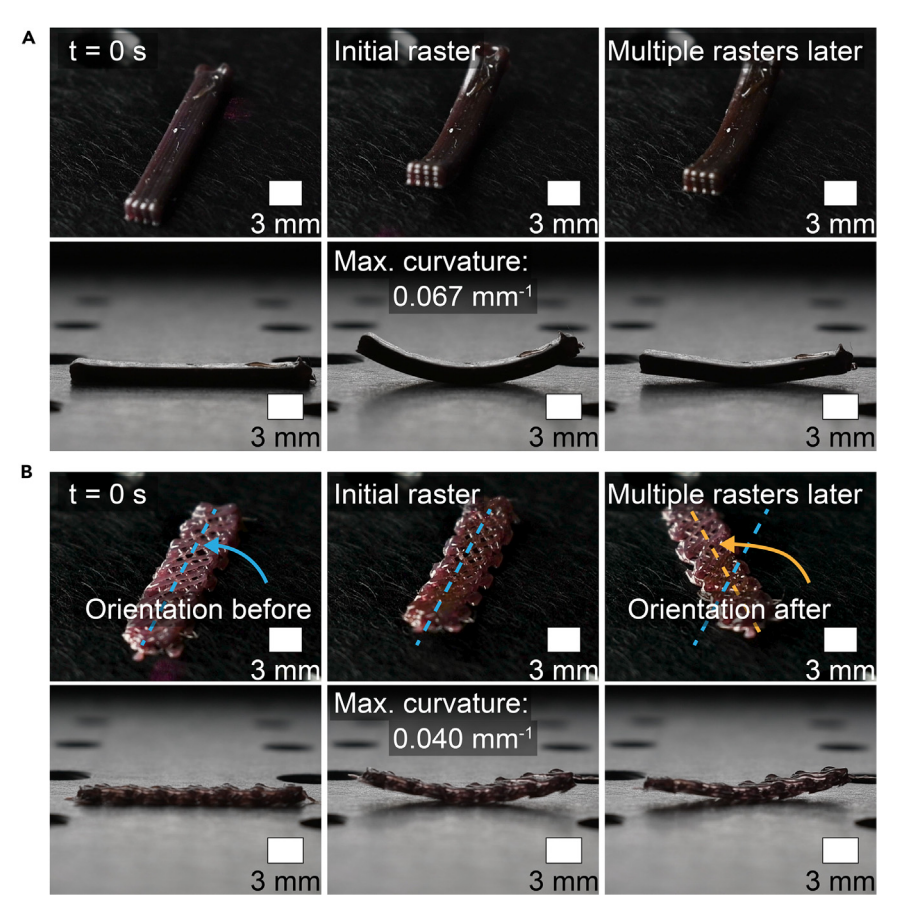


Figure 7. Photoresponsive actuation differences between AuNR-filled LCE solid bars and printed architectures

(A) Sequential images of a solid bar as it is subjected to photothermal actuation. The solid bar initially bends and then shrinks as heat conducts through the sample. A top view (top) and side view (bottom) are shown.

(B) Sequential images of a  $45^{\circ}$  lattice as it is subjected to photothermal actuation. The lattice bends but also rotates in the plane of the surface after multiple rasters of the laser. A top view (top) and side view (bottom) are shown. The dashed lines highlight the rotation of the composite.

of the 45° lattice, which rotated as the stimulus moved across the composite (Figure 7B; Video S5). Next, we aimed to combine the asymmetric absorption stimulus and further introduce additional complexity into the geometric structures to demonstrate actuation modes like bending, twisting, and rolling.

Other structures were printed that exhibited interesting photothermal responsivity. These structures were selected to capitalize on the advantages of DIW: larger lattice structures with overhangs, coiled strands, and a tall, single-filament cylinder. As described, these structures demonstrate movement that would be useful for soft machines, including bending, crawling, and rolling. When the laser was incident upon a lattice structure, the pores between the strands of ink contracted in the location of the laser (Figure 8A; Video S6). Note that at high incident laser power, the temperature could easily exceed 150°C, and smoke could be observed, indicating damage to the sample. However, by controlling the incident dose, the structure could actuate repeatedly and avoid damage. We rastered the laser across the composite 100 times, and the composite reached a steady state of continued actuation where the corners lifted as the composite contracted (Figure 8B; Video S6). Notably, the



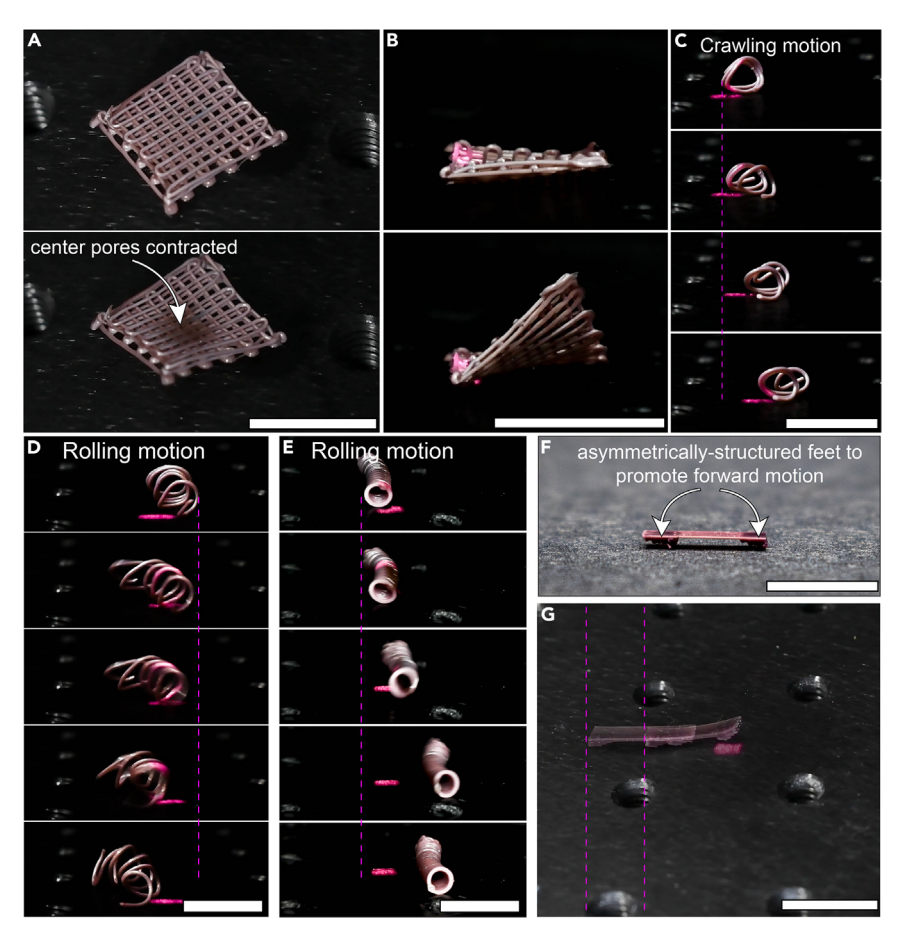


Figure 8. Photothermal actuation response of different printed AuNR-filled LCE architectures

- (A) Localized photothermal responsivity of a lattice structure where the center pores contracted (bottom image) when the center portion was exposed to laser light.
- (B) Photothermal responsivity of a lattice structure results in actuation modes like this contraction that lifts the corner up off the surface as the laser rasters.
- (C) Successive video frames of a composite that is slowly crawling as the laser is rastered across the left edge of the material.
- (D and E) Successive video frames of a coil (D) and a cylinder (E) composite that roll following rastering.
- (F) Photograph of a crawler that was designed to have asymmetric friction for forward motion.
- (G) Sequential photographs overlaid showing the crawler move forward following laser rastering. Dashed lines are for reference of starting and ending points. The scale bars in all images represent 15 mm.

light impinges upon the composite asymmetrically, resulting in curvature. <sup>51,52</sup> The light is absorbed by the top layer first, so this top layer undergoes shape morphing initially. As this top layer contracts, the bottom layer can deform, which results in a repeatable bending and unbending motion. Any transmitted light and diffusely scattered light could impinge upon the bottom layers, which would occur at a slower rate. Alternatively, subsequent layers that are in physical contact could transmit heat. These features of these composites offer another degree of control for actuation, where the architecture of the composite could be designed to undergo multiple stages of motion.

A coiled strand was also printed by printing a cylindrical base to adhere the coil to the surface and then printing in a free-form helical pattern. This coiled strand



exhibited interesting photoresponsivity that enabled different modes of motion depending on the incident light and sample geometry. If the laser rastered across the structure, the composite exhibited stochastic motion (Video S7). If the laser rastered on one edge of the coil, the coil could slowly crawl forward (Figure 8C; Video S7). The coil could also roll; this rolling motion appeared to occur more frequently when either end of the coil was able to push against the surface to propel the coil forward (Figure 8D; Video S7). The coil could roll with and without the base, which was removed for some experiments to see the effect on actuation. Overall, these unique modes of motion and actuation demonstrate the potential of utility of these photoresponsive composites.

A printed cylinder could also roll when subjected to localized light (Figure 8D; Video S8). In this case, the printed cylinder would heat to temperatures above 100°C and bend; this bending would be followed by a rapid motion as the cylinder became unbalanced, pushing the cylinder forward. The cylinder could roll multiple times. In some cases, the composite would appear to start emitting smoke as it reached elevated temperatures, followed by the cylinder rolling away from the light. As the photothermal stimulus impinges upon the sample, the composite actuates and rolls away from the stimulus. Recent perspectives on soft material/machine design highlight and describe the concept of physical intelligence, where materials are designed to exhibit similar behavior (e.g., damage avoidance). 1,2,53 Such behavior manifests while machine complexity is reduced to a simple printed composite material, relative to traditional machines that have on-board sensing and computation. Finally, a mass like a wire could also be placed into the hollow cylinder. The cylinder could also roll while carrying this mass (Video S8), demonstrating work potential.

A photoresponsive crawler could also be designed and printed. For this crawler, asymmetry was introduced so that the crawler would be subjected to asymmetric friction during photothermal actuation, which would propel the crawler forward (Figure 8F), similar to previous designs in literature. 54 Multiple geometries were considered, including three different body lengths (12, 17, and 22 mm), two different body thicknesses (one or two layers), and two different body widths (six or eight strands wide). The crawler with a body length of 12 mm did not crawl forward (Video S9). The first layer of the feet comprised 75% of the body length and may have restricted motion of the body that would have propelled the crawler forward. The crawlers with body lengths of 17 and 22 mm were able to crawl forward (Figure 8G; Video S9). The body thickness and width of these crawlers were two layers and eight strands, respectively. A crawler with a body thickness of one layer and a different crawler with a body thickness of two layers but a width of six strands were not stable during actuation and would flip onto their side or back (Video S7). Overall, these crawlers highlight the ability to leverage achievable variation in print architecture and photothermal actuation to design and fabricate simple soft machines.

Considering movement with light, the printed cylinder that can roll appeared promising to achieve fast motion. We used computer vision to track the motion of printed cylinders and concomitantly controlled the position of the laser that rastered across the sample. In this case, the cylinder could roll forward at an average rate of 1.8 mm/s. For comparison, an LCE actuator that could walk across a ratcheted surface moved at a rate of 0.24 mm/s, and a rover on Mars can move at about 42 mm/s<sup>46,55</sup> Tracking of the cylinder revealed that the cylinder would sometimes roll forward followed by rolling backward slightly as it lost momentum (Figures 9A and 9B; Video \$10). During this rolling motion, the velocity could exceed 5 mm/s. By biasing the incident light to one side of the actuator, the direction of rolling could



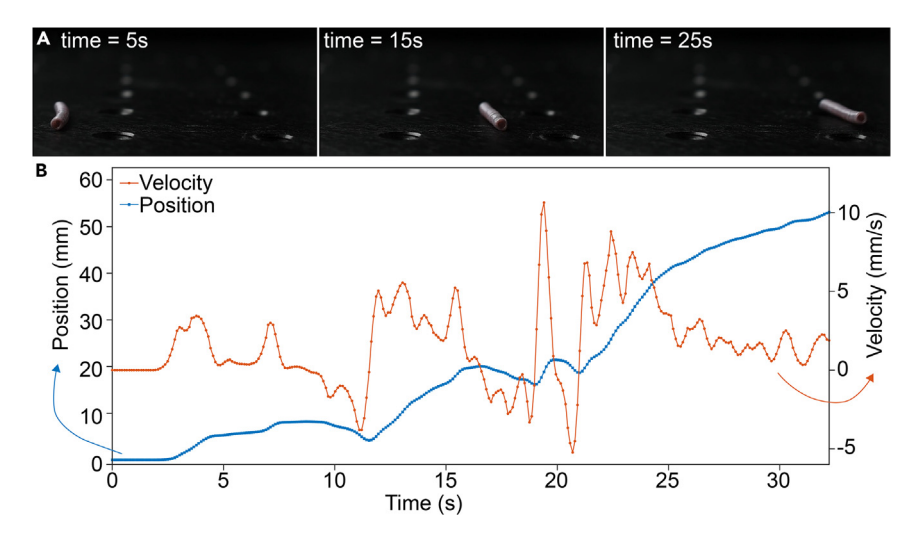


Figure 9. Computer vision control of printed cylinder rolling direction

(A) Screen captures of Video S10, where a rolling cylinder continues to roll as its position is tracked, and the laser is continuously moved to raster the edge of the cylinder.

(B) Position and velocity tracking of the cylinder that is continuously rolling.

be controlled, allowing the cylinder to roll back and forth across the surface (Video S10).

#### **Conclusions**

We examined LC oligomer synthesis and processing and their effect on compatibility with AuNRs and amenability to DIW. Overall, there are many factors to consider when developing formulations that can be reliably printed, including molecular weight distribution, which may be affected by synthesis and processing; residual solvent content if solvent is used in synthesis; and curing kinetics. Even after considering these parameters, the printability of composites also relies on the compatibility of the composite filler with the matrix. In our consideration of these factors, we highlighted how the molecular weight distribution of thiol-based formulations can be tuned when using solvent processing and controlling monomer addition. These oligomers can cure quickly, which allows for high fidelity in printing. The compatibility of AuNRs is affected by processing as much as it may be affected by chemical differences between thiol-containing and amine-containing inks.

Printed structures with complex shapes can reversibly actuate, and the inclusion of AuNRs allows for photoresponsivity that displays unique actuation and motion. The soft machines that we fabricated with these materials could repeatably oscillate between bending angles, crawl either through designed structures or through localized heating, roll due to pushing or change in balance, and transport mass. The movement that was observed results from a unique combination of architecture and LCE alignment that is controlled by DIW, absorption and subsequent photothermal heating that is enabled by the presence of AuNRs, and thermal transport that is determined by the printed geometry and material properties. Furthermore, the movement could vary depending on the rastering pattern of the laser. The combination and interplay of these factors present an interesting challenge to prescribe novel modes of motion in these materials.

Our initial attempts to control the motion of these soft machines resulted in rolling motion, where the direction of rolling depended on the position of the laser. This

## **Matter** Article



rolling motion could be continuous when tracking the position of the roller and subsequently repositioning the laser to continuously impinge upon the sample. This motion and other examples that we demonstrated resembled intelligent behavior: damage avoidance. As the sample absorbed light and heated, it would roll away from the light to avoid overheating that could cause burning. In this case, the material enables sensing of its local environment and responsivity along with locomotion, which is a promising step toward more intelligent soft machines. These results will be important to guide others in developing new, photoresponsive LCEs for multifunctional materials, soft machines, and engineered devices. The ability to achieve movement with light could eventually be used in more complex machines, such as those for walking and interacting with our environment.

#### **EXPERIMENTAL PROCEDURES**

#### Resource availability

#### Lead contact

Further information and requests for resources and materials should be directed to and will be fulfilled by the lead contact, Caitlyn C. Cook (krikorian3@llnl.gov).

#### Materials availability

This study did not generate new unique reagents.

#### Data and code availability

Additional experimental data and code are available upon reasonable request to the authors.

#### LC oligomer synthesis and ink processing

LC oligomers were the primary component of all inks that were studied. For oligomers that contained thiol-based monomers, we followed the following synthetic route. GDMP (from TCI) was diluted in DCM (from Thermo Fisher Scientific; typical concentration of about 4 wt %). The LC monomer (RM82 or RM257, from Ambeed or Wilshire) was dissolved in solvent (DCM or MEK) in a separate vessel to a typical concentration of about 8 wt %. The base catalyst, DBU (from Thermo Fisher Scientific), was added to the flask that contained the thiol-based monomer to a final concentration of 1 wt % relative to the total mass of the monomers.

While the contents of the flask that contained the thiol-based monomer were stirred, the solution that contained the LC monomer was slowly added dropwise. For example, the addition of the LC monomer could occur over a period of about 10–20 min. A glass dropping funnel that remained closed to the ambient atmosphere was used to avoid the evaporation of solvent; the evaporation of solvent would allow the LC monomer to precipitate from solution.

The reaction proceeded for about 16 h before the base catalyst was removed by washing with a 1 M solution of hydrochloric acid, followed by washing with deionized water. This washing process was repeated once. The organic phase was separated, dried with magnesium sulfate, and filtered. Butylated hydroxytoluene (BHT) was added at a concentration of 0.2 wt % relative to the total oligomer concentration. Solvent was removed using a rotary evaporator; typically, the oligomer was dried under vacuum at 70°C for 3 h.

After the removal of solvent, the PI, 2,2-dimethoxy-2-phenylacetophenone (DMPA), was added; formulations contained 2 wt % DMPA unless otherwise noted. For the





Th-LCEs, the remaining LC monomer was also added after the removal of solvent using heating and shear mixing.

For oligomers that contained amine-based monomers, PI and inhibitor were added to a reaction vessel. The reaction vessel was attached to a reflux column and heated to 90°C. Polymerization proceeded for >12 h.

#### Ink characterization

The reaction kinetics of the oligomer formation was monitored using a Mettler Toledo ReactRaman 785 spectrometer. A Fiber BallProbe probe with a diameter of 9.5 mm was used. The laser power was 300 mW, and spectra were measured from 3,200 to 100 cm<sup>-1</sup>. For each measurement, 20 scans were taken with a 1 s exposure. The iC Raman 7.1 software was used for initial data smoothening, solvent correction, and baseline subtraction of the signal. Integration of the peak of interest was performed using MATLAB R2022a.

The molecular weight of the oligomers was characterized using an SEC system (Wyatt Technology) that included a MALS detector and refractive index detector. First, a sample of the formulation was dissolved in 2-butanone (Sigma) to a final polymer concentration of 3.0–3.2 mg/mL. Samples were stirred for at least 16 h before measurement. The solution was filtered through a 0.2  $\mu$ m syringe filter. Then, 100  $\mu$ L of sample was injected into a set of four columns (Agilent PL-Gel 10  $\mu$ m mixed B), which were connected to the detectors. The columns and detectors were set to 40°C.

To determine the molecular weight, the polymer's dRI relative to its concentration (dn/dc) must be known. We assumed that 100% of the injected sample reached the detectors and thus determined dn/dc using the refractive index detector. The molecular weight of some oligomers may be near the limit of quantification of our detectors, and the dn/dc may be affected by the relative fraction of each monomer in a given oligomer. Thus, we use the molecular weight quantification to make qualitative assessments and to compare the effects of various synthesis and processing modifications.

The conversion of acrylate groups in the oligomers was monitored using a near-IR fast-scanning Fourier transform IR (FTIR) spectrometer (Bruker Vertex 80). Samples were sandwiched between two glass slides and separated by glass spacers with a thickness of 160  $\mu m$ . Samples were irradiated using an OmniCure S2000 light source, and the surface power density of the light was measured prior to each experiment using a ThorLabs S120VC sensor. The acrylate functional units of the formulations exhibit a peak in the near IR at  $\approx$  6,160 cm $^{-1}$  (Figure S6A). The area of this peak was used to determine the conversion kinetics, where the initial area was taken as 0% conversion. For monitoring residual solvent, a PerkinElmer Spectrum GX FTIR system was used.

The thermal properties of LC formulations were characterized using DSC using a Discovery DSC 2500 from TA Instruments. Samples were heated to  $120^{\circ}$ C and then cooled to  $-40^{\circ}$ C at  $20^{\circ}$ C min<sup>-1</sup>; this cycle was repeated three times. The second heating ramp was used to determine the peak positions of the transitions. For modulated DSC (mDSC), the sample was heated to  $120^{\circ}$ C in a DSC pan before testing; then, the temperature of the sample was equilibrated at  $-50^{\circ}$ C. Using a modulation of  $0.5^{\circ}$ C over 60 s, the sample was heated to  $150^{\circ}$ C at  $1^{\circ}$ C min<sup>-1</sup>.

## **Matter** Article



A DHR-3 rheometer (TA Instruments) was used for rheological characterization. Formulations were characterized with steady shear and oscillatory tests. For steady shear measurements, a 2° cone plate geometry that is 40 mm in diameter was used. Samples were heated to 60°C for 3 min, followed by equilibration at 25°C while holding a shear rate of 0.11 s<sup>-1</sup>. Then, the shear rate was increased to 500 s<sup>-1</sup> while collecting data in between. For oscillatory measurements, cross-hatched parallel plates that were 25 mm in diameter were used to measure temperature-dependent oscillatory moduli, and disposable parallel plates that were 20 mm in diameter were used for stability tests. An oscillation of 0.5% at 1 s<sup>-1</sup> was maintained while heating from 0°C to 95°C, followed by a reversed temperature ramp.

#### **Direct ink writing**

For printing, the inks were deposited into a stainless-steel syringe barrel. The barrel was capped and centrifuged to remove air bubbles. A syringe piston was placed against the top of the ink. A stainless-steel nozzle from Tecdia with an inner diameter of about 500  $\mu m$  was used when printing. For extrusion, an Ultimus V pressure box (Nordson EFD) was used, which can provide pressure up to 100 psi.

During extrusion, the ink was irradiated using an OmniCure S2000 light source, and the surface power density of the light was measured using a ThorLabs S120VC sensor. The position of the light source was fixed for most geometries; however, for some geometries, like the lattice structure, the position had to be manually moved, as the printing head or the printed part could create a shadow and hinder curing. The surface power density was between 3 and 20 mW cm $^{-2}$ , depending on the formulation and printing parameters. Printing parameters were optimized heuristically for a given formulation. An example of printing parameters that was used for the 30 layer wall was a pressure of 20 psi, a nozzle diameter of 500  $\mu m$ , and a nozzle speed of 8 mm/s. The layer height was set to 90% of the nozzle diameter. An Aerotech ANT 130-XY and 130-L-Z5 axis stage was controlled via an A3200 controller through an Aerotech A3200 CNC operator interface. The print paths were generated using custom slicing programs.

#### **Materials characterization**

The actuation characteristics were measured by dynamic mechanical analysis (DMA) using a Discovery DMA 850 from TA Instruments. Printed rectangular pieces that were about 25 mm in length, between 2 and 3 mm in width, and one to three layers in thickness (between 0.4 and 1.4 mm) were used in isostress tests. The samples were placed in a tension geometry, and the input tension was held at 0 MPa as the temperature was increased above the  $T_{\rm NI}$  at a rate of  $10^{\circ} {\rm C~min^{-1}}$ . The temperature was decreased to  $0^{\circ} {\rm C}$  and then increased once more. Actuation strain values were determined from the sample length at  $120^{\circ} {\rm C}$  relative to the length at  $20^{\circ} {\rm C}$  based on data from the second heating step. Stress-strain characteristics were measured using an Instron universal testing machine, and thin films of cast samples with and without AuNRs were tested for comparison.

Photographs were taken using a Nikon D750 camera. Exposure, tone, contrast, clarity, and noise reduction were adjusted globally using Adobe Lightroom. Thermal images were taken using a FLIR C5 thermal camera.

#### Inks with AuNRs

AuNRs were synthesized following a previously published seed-mediated technique. <sup>56</sup> We targeted a localized surface plasmon resonance of 800 nm and





dimensions of 78  $\times$  21 nm. Initially, these AuNRs were stabilized with cetyltrimethy-lammonium bromide (CTAB). In a typical scale of 1 L, the CTAB-stabilized AuNRs contain  $\approx$ 190 mg of Au. Before purification, the concentration of CTAB was 90 mM. Functionalization of AuNRs with PEG-thiol (Sigma, molecular weight of 6,000 g/mol) requires reducing the CTAB concentration below 1 mM. A typical functionalization procedure as well as characterization are described below and outlined in Figure S12.

One hundred milliliters of the as-synthesized CTAB-stabilized AuNRs was purified by centrifugation twice at up to 12,500 rpm for 20 min to reduce the CTAB concentration. After the first round of centrifugation, more than 99 mL of the supernatant was removed without disturbing the AuNR pellet at the bottom of the centrifuge tubes. Ninety-nine milliliters of water was added to the AuNR pellet, and the AuNRs were redispersed. After the second round of purification, most of the supernatant ( $\approx$ 99 mL) was discarded, and then 5 mL of water was added to redisperse the AuNRs.

The concentrated AuNR solution was then added to 5 mL of water containing 20 mg of PEG-thiol. The solution was sonicated briefly and kept at 40°C for 24 h with mild stirring at 200 rpm. We repeated the centrifuging and decanting steps outlined above, except that we replaced the  $H_2O$  with organic solvent. In some cases, 15 mL of ethanol and 15 mL of hexane were added to the AuNR solution to drive floculation. In these cases, the AuNRs were redispersed in ethanol and hexane separately. The PEG-AuNR pellet was then redispersed in 10 mL organic solvent (e.g., DCM), yielding a concentration of  $\approx$ 1.9 mg/mL AuNRs. After each centrifuging step, the optical density of the decanted layers was measured using UV-vis spectroscopy for one batch of AuNR purification. A Shimadzu UV-2401 UV-vis spectrometer was used.

To disperse the AuNRs in the LC oligomers, the LC oligomers in solvent were mixed with the AuNRs following the functionalization of the AuNRs. The solution was placed in an open container in a fume hood for about 16 h, and the solvent mostly evaporated. The formulation was completed by drying under vacuum at 70°C for 3 h.

For photothermal actuation, the AuNR-LCE composites were subjected to a custom-built 808 nm 3,000 mW laser. The laser was powered using an LSR-PS-II (CivilLaser) and had a beam size of  $5.5 \times 5.5$  mm at the aperture. The surface power density of the laser could be tuned by the power supply, and a photometer was used to calibrate the power. The laser could raster across the surface of the sample using LabVIEW to control the position of two scanning galvo systems (GVS002, Thorlabs). Typically, the laser was rastered across the sample at a rate between 3 and 100 mm/s.

To characterize photothermal actuation, the actuation was recorded, and curvature was analyzed using Kappa, a curvature analysis package in ImageJ. The surface temperature was recorded using a FLIR C5 thermal camera. For specific work density measurements, one end of the solid bar was affixed to the surface of the laser table, and a weight was attached to the other end. The height to which the weight was lifted was measured, and the mass of the weight was recorded to determine the total work. The work was normalized to the sample mass to determine the specific work density (Figure S13).



For the tracking of the position of the cylinder, MATLAB was used to determine the location of the cylinder and to control the position of the laser. An example of image processing (Figure S14) shows how the laser position was offset from the center of the tracked cylinder to enable forward motion. MATLAB was also used to track the position over time to calculate the velocity of the cylinder.

#### SUPPLEMENTAL INFORMATION

Supplemental information can be found online at https://doi.org/10.1016/j.matt. 2024.01.006.

#### **ACKNOWLEDGMENTS**

This work was performed under the auspices of the US Department of Energy by Lawrence Livermore National Laboratory under contract DE-AC52-07NA27344, LDRD tracking number 22-ERD-030, release number LLNL-JRNL-847088. This work was also supported by the National Science Foundation grant CMMI-1763025 and the Harvard MRSEC (DMR-2011754). We also acknowledge partial support from the National Science Foundation through the DMR/POL program, number DMR-2104841 (to S.Y.).

#### **AUTHOR CONTRIBUTIONS**

J.B.T., J.A.L., S.Y., E.L., and C.C.C. conceived ideas and supervised experiments. M.J.F. synthesized LCEs, characterized synthetic and curing kinetics, characterized molecular weight, characterized rheological properties, printed components, and tested photothermal actuation. D.H.P. and R.T. characterized thermal and actuation properties. R.T. and J.A.M. printed components. Y.W. assisted with materials synthesis, characterization, and AuNR processing. M.H.R. synthesized AuNRs and helped with AuNR processing. C.K.L. helped with molecular weight characterization. B.D.M. designed and built the 808 nm laser and helped with photothermal characterization. M.J.F., E.L., and C.C.C. wrote the manuscript. All authors discussed and edited the manuscript.

#### **DECLARATION OF INTERESTS**

The authors declare no competing interests.

Received: March 15, 2023 Revised: November 21, 2023 Accepted: January 9, 2024 Published: February 2, 2024

#### **REFERENCES**

- 1. Sitti, M. (2021). Physical intelligence as a new paradigm. Extreme Mech. Lett. 46, 101340.
- Ford, M.J., Ohm, Y., Chin, K., and Majidi, C. (2022). Composites of functional polymers: Toward physical intelligence using flexible and soft materials. J. Mater. Res. 37, 2–24.
- Liu, K., Tebyetekerwa, M., Ji, D., and Ramakrishna, S. (2020). Intelligent Materials. Matter 3, 590–593.
- 4. The Material Is the Machine; 2005. 1100892.
- McCracken, J.M., Donovan, B.R., and White, T.J. (2020). Materials as Machines. Adv. Mater. 32, 1906564.
- Ula, S.W., Traugutt, N.A., Volpe, R.H., Patel, R.R., Yu, K., and Yakacki, C.M. (2018). Liquid crystal elastomers: an introduction and review of emerging technologies. Liq. Cryst. Rev. 6, 78–107.
- Li, Y., Parlato, G., Masese, F.K., Kasi, R.M., Zhang, T., and Wang, X. (2022). Morphing of stiffness-heterogeneous liquid crystal elastomers via mechanical training and locally controlled photopolymerization. Matter 5, 4332–4346.
- 8. Huang, X., Ford, M., Patterson, Z.J., Zarepoor, M., Pan, C., Majidi, C., and Majidi, C. (2020). Shape memory materials for electrically-

- powered soft machines. J. Mater. Chem. B 8, 4539–4551.
- Wang, Y., Liu, J., and Yang, S. (2022). Multifunctional liquid crystal elastomer composites. Appl. Phys. Rev. 9, 011301.
- Jiang, H., Kelch, S., and Lendlein, A. (2006). Polymers Move in Response to Light. Adv. Mater. 18, 1471–1475.
- Zhai, F., Feng, Y., Li, Z., Xie, Y., Ge, J., Wang, H., Qiu, W., and Feng, W. (2021). 4D-printed untethered self-propelling soft robot with tactile perception: Rolling, racing, and exploring. Matter 4, 3313–3326.

## **CellPress**

## Matter Article

- Zeng, H., Wasylczyk, P., Wiersma, D.S., and Priimagi, A. (2018). Light Robots: Bridging the Gap between Microrobotics and Photomechanics in Soft Materials. Adv. Mater. 30, 1703554.
- Wie, J.J., Shankar, M.R., and White, T.J. (2016). Photomotility of polymers. Nat. Commun. 7, 13260.
- Palagi, S., Mark, A.G., Reigh, S.Y., Melde, K., Qiu, T., Zeng, H., Parmeggiani, C., Martella, D., Sanchez-Castillo, A., Kapernaum, N., et al. (2016). Structured light enables biomimetic swimming and versatile locomotion of photoresponsive soft microrobots. Nat. Mater. 15, 647–653.
- Yu, Y., Nakano, M., and Ikeda, T. (2003). Directed bending of a polymer film by light. Nature 425, 145.
- Camacho-Lopez, M., Finkelmann, H., Palffy-Muhoray, P., and Shelley, M. (2004). Fast liquidcrystal elastomer swims into the dark. Nat. Mater. 3, 307–310.
- White, T.J., Tabiryan, N.V., Serak, S.V., Hrozhyk, U.A., Tondiglia, V.P., Koerner, H., Vaia, R.A., Bunning, T.J., Bunning, J., and T.. (2008). A high frequency photodriven polymer oscillator. Soft Matter 4, 1796–1798.
- Dong, L., and Zhao, Y. (2018). Photothermally driven liquid crystal polymer actuators. Mater. Chem. Front. 2, 1932–1943.
- Han, D.-D., Zhang, Y.-L., Ma, J.-N., Liu, Y.-Q., Han, B., and Sun, H.-B. (2016). Light-Mediated Manufacture and Manipulation of Actuators. Adv. Mater. 28, 8328–8343.
- Yang, L., Setyowati, K., Li, A., Gong, S., and Chen, J. (2008). Reversible Infrared Actuation of Carbon Nanotube–Liquid Crystalline Elastomer Nanocomposites. Adv. Mater. 20, 2271–2275.
- Kohlmeyer, R.R., and Chen, J. (2013). Wavelength-Selective, IR Light-Driven Hinges Based on Liquid Crystalline Elastomer Composites. Angew. Chem. Int. Ed. 52, 9234–9237.
- Ji, Y., Huang, Y.Y., Rungsawang, R., and Terentjev, E.M. (2010). Dispersion and Alignment of Carbon Nanotubes in Liquid Crystalline Polymers and Elastomers. Adv. Mater. 22, 3436–3440.
- Kim, H., Lee, J.A., Ambulo, C.P., Lee, H.B., Kim, S.H., Naik, V.V., Haines, C.S., Aliev, A.E., Ovalle-Robles, R., Baughman, R.H., and Ware, T.H. (2019). Intelligently Actuating Liquid Crystal Elastomer-Carbon Nanotube Composites. Adv. Funct. Mater. 29, 1905063.
- 24. Yang, M., Xu, Y., Zhang, X., Bisoyi, H.K., Xue, P., Yang, Y., Yang, X., Valenzuela, C., Chen, Y., Wang, L., et al. (2022). Bioinspired Phototropic MXene-Reinforced Soft Tubular Actuators for Omnidirectional Light-Tracking and Adaptive Photovoltaics. Adv. Funct. Mater. 32, 2201884.
- (2019). A multifunctional shape-morphing elastomer with liquid metal inclusions. Proc. Natl. Acad. Sci. USA.
- **26.** Ford, M.J., Palaniswamy, M., Ambulo, C.P., Ware, T.H., and Majidi, C. (2020). Size of liquid

- metal particles influences actuation properties of a liquid crystal elastomer composite. Soft Matter 16, 5878–5885.
- Zheng, J., Cheng, X., Zhang, H., Bai, X., Ai, R., Shao, L., and Wang, J. (2021). Gold Nanorods: The Most Versatile Plasmonic Nanoparticles. Chem. Rev. 121, 13342–13453.
- Yang, H., Liu, J.-J., Wang, Z.-F., Guo, L.-X., Keller, P., Lin, B.-P., Sun, Y., and Zhang, X.-Q. (2015). Near-infrared-responsive gold nanorod/liquid crystalline elastomer composites prepared by sequential thiolclick chemistry. Chem. Commun. 51, 12126– 12129.
- Yang, X., Chen, Y., Zhang, X., Xue, P., Lv, P., Yang, Y., Wang, L., and Feng, W. (2022). Bioinspired light-fueled water-walking soft robots based on liquid crystal network actuators with polymerizable miniaturized gold nanorods. Nano Today 43, 101419.
- Lv, P., Yang, X., Bisoyi, H.K., Zeng, H., Zhang, X., Chen, Y., Xue, P., Shi, S., Priimagi, A., Wang, L., et al. (2021). Stimulus-driven liquid metal and liquid crystal network actuators for programmable soft robotics. Mater. Horiz. 8, 2475–2484.
- Lu, X., Zhang, H., Fei, G., Yu, B., Tong, X., Xia, H., and Zhao, Y. (2018). Liquid-Crystalline Dynamic Networks Doped with Gold Nanorods Showing Enhanced Photocontrol of Actuation. Adv. Mater. 30, 1706597.
- Herbert, K.M., Fowler, H.E., McCracken, J.M., Schlafmann, K.R., Koch, J.A., and White, T.J. (2021). Synthesis and alignment of liquid crystalline elastomers. Nat. Rev. Mater. 7, 23–38.
- del Pozo, M., Sol, J.A.H.P., Schenning, A.P.H.J., and Debije, M.G. (2022). 4D Printing of Liquid Crystals: What's Right for Me? Adv. Mater. 34, 2104390.
- Ambulo, C.P., Burroughs, J.J., Boothby, J.M., Kim, H., Shankar, M.R., and Ware, T.H. (2017). Four-dimensional Printing of Liquid Crystal Elastomers. ACS Appl. Mater. Interfaces 9, 37332–37339.
- Kotikian, A., Truby, R.L., Boley, J.W., White, T.J., and Lewis, J.A. (2018). 3D Printing of Liquid Crystal Elastomeric Actuators with Spatially Programed Nematic Order. Adv. Mater. 30, 1706164.
- López-Valdeolivas, M., Liu, D., Broer, D.J., and Sánchez-Somolinos, C. (2018). 4D Printed Actuators with Soft-Robotic Functions. Macromol. Rapid Commun. 39, 1700710.
- Kuang, X., Roach, D.J., Wu, J., Hamel, C.M., Ding, Z., Wang, T., Dunn, M.L., and Qi, H.J. (2019). Advances in 4D Printing: Materials and Applications. Adv. Funct. Mater. 29, 1805290.
- Kotikian, A., McMahan, C., Davidson, E.C., Muhammad, J.M., Weeks, R.D., Daraio, C., and Lewis, J.A. (2019). Untethered soft robotic matter with passive control of shape morphing and propulsion. Sci. Robot. 4, eaax7044.
- **39.** Roach, D.J., Sun, X., Peng, X., Demoly, F., Zhou, K., and Qi, H.J. (2022). 4D Printed

- Multifunctional Composites with Cooling-Rate Mediated Tunable Shape Morphing. Adv. Funct. Mater. 32, 2203236.
- Li, Y., Yu, H., Yu, K., Guo, X., and Wang, X. (2021). Reconfigurable Three-Dimensional Mesotructures of Spatially Programmed Liquid Crystal Elastomers and Their Ferromagnetic Composites. Adv. Funct. Mater. 31, 2100338.
- Kotikian, A., Morales, J.M., Lu, A., Mueller, J., Davidson, Z.S., Boley, J.W., and Lewis, J.A. (2021). Innervated, Self-Sensing Liquid Crystal Elastomer Actuators with Closed Loop Control. Adv. Mater. 33, 2101814.
- Ambulo, C.P., Ford, M.J., Searles, K., Majidi, C., and Ware, T.H. (2021). 4D-Printable Liquid Metal-Liquid Crystal Elastomer Composites. ACS Appl. Mater. Interfaces 13, 12805–12813.
- 43. Wu, Z., Liu, L., Cheng, P., Fang, J., Xu, T., and Chen, D. (2019). Reusable gold nanorod/liquid crystalline elastomer (GNR/LCE) composite films with UV-triggered dynamic crosslinks capable of micropatterning and NIR actuation. J. Mater. Chem. C 7, 14245–14254.
- 44. Wang, Y., Dang, A., Zhang, Z., Yin, R., Gao, Y., Feng, L., and Yang, S. (2020). Repeatable and Reprogrammable Shape Morphing from Photoresponsive Gold Nanorod/Liquid Crystal Elastomers. Adv. Mater. 32, 2004270.
- Yeung, K.-W., Dong, Y., Chen, L., Tang, C.-Y., Law, W.-C., Tsui, G.C.-P., and Engstrøm, D.S. (2020). Printability of photo-sensitive nanocomposites using two-photon polymerization. Nanotechnol. Rev. 9, 418–426.
- Wang, Y., Yin, R., Jin, L., Liu, M., Gao, Y., Raney, J., and Yang, S. (2023). 3D-Printed Photoresponsive Liquid Crystal Elastomer Composites for Free-Form Actuation. Adv. Funct. Mater. 33, 2210614.
- Chen, L., Dong, Y., Tang, C.-Y., Zhong, L., Law, W.-C., Tsui, G.C.P., Yang, Y., and Xie, X. (2019). Development of Direct-Laser-Printable Light-Powered Nanocomposites. ACS Appl. Mater. Interfaces 11, 19541–19553.
- 48. Xia, Y., Zhang, X., and Yang, S. (2018). Instant Locking of Molecular Ordering in Liquid Crystal Elastomers by Oxygen-Mediated Thiol—Acrylate Click Reactions. Angew. Chem. Int. Ed. *57*, 5665–5668.
- Guo, Y., Lee, J., Son, J., Ahn, S.k., Carrillo, J.-M.Y., and Sumpter, B.G. (2019). Decoding Liquid Crystal Oligomer Phase Transitions: Toward Molecularly Engineered Shape Changing Materials. Macromolecules 52, 6878–6888.
- McCracken, J.M., Donovan, B.R., Lynch, K.M., and White, T.J. (2021). Molecular Engineering of Mesogenic Constituents Within Liquid Crystalline Elastomers to Sharpen Thermotropic Actuation. Adv. Funct. Mater. 31, 2100564.
- Qian, X., Zhao, Y., Alsaid, Y., Wang, X., Hua, M., Galy, T., Gopalakrishna, H., Yang, Y., Cui, J., Liu, N., et al. (2019). Artificial phototropism for omnidirectional tracking and harvesting of light. Nat. Nanotechnol. 14, 1048–1055.

## **Matter** Article



- **52.** (2019). Soft phototactic swimmer based on self-sustained hydrogel oscillator. Sci. Robot.
- 53. Howard, D., Eiben, A.E., Kennedy, D.F., Mouret, J.-B., Valencia, P., and Winkler, D. (2019). Evolving embodied intelligence from materials to machines. Nat. Mach. Intell. 1, 12–19.
- Bandari, V.K., and Schmidt, O.G. (2021).
   System-Engineered Miniaturized Robots: From Structure to Intelligence. Adv. Intell. Syst. 3, 2000284.
- Rankin, A., Maimone, M., Biesiadecki, J., Patel, N., Levine, D., and Toupet, O. (2020). Driving Curiosity: Mars Rover Mobility Trends during
- the First Seven Years. In 2020 IEEE Aerospace Conference, pp. 1–19.
- 56. Kozek, K.A., Kozek, K.M., Wu, W.-C., Mishra, S.R., and Tracy, J.B. (2013). Large-Scale Synthesis of Gold Nanorods through Continuous Secondary Growth. Chem. Mater. 25, 4537–4544.